GDCh

Research Article

Angewandte
Chemie
International Edition
www.angewandte.org

Electrocatalysis

Highly Selective Oxygen Electroreduction to Hydrogen Peroxide on Sulfur-Doped Mesoporous Carbon

Juan Du, Yicheng Liu, Ming Sun, Jing Guan,* Aibing Chen,* and Buxing Han*

Abstract: As a paradigm-shifting material platform in energy catalysis, precisely engineered ordered mesoporous carbon spheres emerge as supreme metal-free electrocatalysts, outperforming conventional carbon-based counterparts through synergistic structural and electronic innovations. Herein, we architecturally design vertically aligned cylindrical mesoporous carbon spheres with atomic-level sulfur doping (S-mC) that establish unprecedented performance benchmarks in the two-electron oxygen reduction reaction ($2e^-$-ORR) to hydrogen peroxide. Systematic comparative studies reveal that the S-mC catalysts achieve exceptional H_2O_2 selectivity (>99%) and activity at current density of -3.5 mA cm^{-2}, surpassing state-of-the-art metal-free catalysts in current density. Impressively, the optimized S-mC electrocatalyst in a flow cell device achieves an exceptional H_2O_2 yield of 25 mol g$_{catalyst}^{-1}$ h^{-1}. The carbon matrix's unique sp^2/sp^3 hybrid network coupled with S-induced charge redistribution generates electron-deficient hotspots that selectively stabilize *OOH intermediates, as evidenced by in situ spectroscopic characterization and DFT calculations. This structural–electronic synergy endows the carbon framework with metal-like catalytic efficiency while maintaining inherent advantages of chemical robustness and cost-effectiveness. The marriage of S-doping engineering with mesoscopic pore architecture control opens a new way for developing efficient carbon-based electrocatalysts for oxygen selective reduction to H_2O_2.

Introduction

Hydrogen peroxide (H_2O_2) is a valuable green chemical oxidant that finds extensive applications in various fields, including chemistry, medicine, industrial production, and daily life.[1–3] It is commonly used for paper and fiber bleaching, chemical synthesis, disinfection, and sewage treatment. In industrial settings, the reduction/oxidation of anthraquinone is typically approached to produce H_2O_2. Although this method is highly efficient for large-scale production, the resulting H_2O_2 is not pure, necessitating the use of expensive solvents and reactants for extraction. Moreover, H_2O_2 is unstable, making long-distance transportation a safety concern. An alternative method for H_2O_2 generation is electrochemical production. Though currently limited by electricity availability, this method has potential for use

in portable and distributed equipment, eliminating transportation safety issues.[4,5] By utilizing an oxygen reduction pathway on the cathode side of a fuel cell, hydrogen peroxide can be produced directly through a two-electron process. This approach overcomes challenges posed by traditional synthesis methods and offers opportunities for employing non-precious metal catalysts. Metal-based catalysts play a critical role in the reduction of O_2 to H_2O_2,[6] but they often encounter issues such as metal particle agglomeration and active site shedding.

The development of a multi-center catalyst utilizing nonmetallic active centers presents a promising solution to the challenges previously mentioned. Nonmetallic active sites offer distinct advantages over traditional metal sites.[7] One key advantage is that multiple nonmetallic active centers can be doped at high levels without the risk of aggregation, even in high-temperature environments. Furthermore, nonmetallic active sites are less susceptible to passivation or etching during catalytic reactions, resulting in improved durability compared to metal-based catalysts. As a result, nonmetallic multi-site catalysts, such as boron, nitrogen, and sulfur-doped carbon, have been successfully implemented in various electrocatalytic processes.[8–11] These catalysts have demonstrated exceptional performance comparable to noble metal catalysts, showcasing their potential for use in two-electron oxygen reduction reaction ($2e^-$-ORR) applications. Notably, sulfur species among nonmetallic active sites have shown high selectivity for $2e^-$-ORR due to their optimal adsorption strength with *OOH species, which is only slightly below the ideal value.

Carbonaceous materials offer a range of advantages, such as affordability, conductivity, and stability, making them a promising catalyst for the electrochemical generation of

[*] J. Du, Y. Liu, M. Sun, A. Chen
College of Chemical and Pharmaceutical Engineering, Hebei
University of Science and Technology, 26 Yuxiang Street,
Shijiazhuang 050018, P.R. China
E-mail: chen_ab@163.com

J. Guan
School of Environmental & Municipal Engineering, Qingdao
University of Technology, Qingdao 266033, P.R. China
E-mail: guanjing@qut.edu.cn

B. Han
Beijing National Laboratory for Molecular Sciences, Institute of
Chemistry, Chinese Academy of Sciences, Beijing 100190, P.R. China
E-mail: hanbx@iccas.ac.cn

⬚ Additional supporting information can be found online in the
Supporting Information section

hydrogen peroxide.[12–14] The catalyst's effectiveness and selectivity are closely tied to the variety of functional groups present on its surface.[15] Introducing sulfur-containing functional groups can boost the performance of carbon-based catalysts in producing hydrogen peroxide via a two-electron pathway. Furthermore, the pore size of carbon materials significantly influences their overall catalytic activity.[1] Porous carbon, in particular, excels in electrocatalysis due to its expansive specific surface area, high pore volume ratio, and superior conductivity. Moreover, porous carbon with a high specific surface area can accommodate a substantial amount of sulfur-containing functional groups, further enhancing its catalytic prowess.[16] Therefore, optimizing the production efficiency of hydrogen peroxide through $2e^-$-ORR can be achieved by adjusting the content and pore size of sulfur-containing functional groups in carbon catalysts.

Based on these considerations, we propose a synergistic effect of sulfur doping modification on mesoporous carbon spheres to enhance the performance of the $2e^-$-ORR process. Theoretical calculations and simulation research indicate that this unique synergy optimizes the adsorption configuration of reactants and intermediates, creating a more favorable reaction environment while reducing kinetic barriers. This results in an H_2O_2 yield of approximately 25 mol $g_{catalyst}^{-1}$ h^{-1}, demonstrating exceptional selectivity and durability. This innovative strategy not only improves $2e^-$-ORR but also opens possibilities for designing advanced catalysts for a range of applications.

Results and Discussion

The manufacture of this material is schematically shown in Figure 1a. Specifically, F127 (as a soft template for forming mesopores) and phenolic resole (as a carbon precursor) were first obtained in a high-temperature aqueous solution (Figure S1). Thiophene was then added to the solution. Thiophene, as a sulfur precursor, was doped into the resin during high-temperature hydrothermal treatment (Figure S2). Then, the obtained product was annealed at 800 °C under the protection of N_2 to obtain the final product, which was denoted as S-mC-x (x = 0, 0.25, 0.375, 0.5, and 1.0, representing the ratio of thiophene to phenolic resole). Details of material manufacturing can be found in the method.

Scanning electron microscope (SEM) was used to analyze the morphology of the S-mC-x samples. The S-mC-0 sample prepared without thiophene (Figure 1) exhibits a homogeneous particle size and a cylindrical pore structure. Introducing thiophene into the reaction system allows to produce mesoporous carbon spheres (S-mC-0.375) with a uniform particle size and ordered mesopore structure, as illustrated in Figure 1d,e. Through transmission electron microscopy (TEM), the regular and ordered mesoporous structure of the spheres is revealed, indicating the presence of more active sites for the catalyst, as shown in Figure 1f. Further examination at high resolution displays the regular mesopores with a diameter of 2.8 nm in Figure 1g, as well as the carbon walls of micropores in Figure 1h. The

ordered mesoporous structure is further confirmed in STEM mode (Figure 1g). Additionally, the introduction of thiophene results in the sulfur doping of the mesoporous carbon within the reaction system. Through EDS mapping, a uniform distribution of C, O, and S within the mesoporous carbon spheres is observed, confirming the successful incorporation of sulfur into the carbon skeleton.

Different from S-mC-0.375, the S-mC-0.25 sample displays a spherical shape with parallel transverse channels, likely impacted by the presence of thiophene in the F127 and resole resin assembly process (Figure 1l,m). However, as the thiophene content continues to increase, the S-mC-0.5 (Figure 1n,o) and S-mC-1.0 (Figure 1p,q) samples exhibit irregular pore structures and some structural breakdown. Figure S3 shows the TEM images of S-mC-0.25, S-mC-0.5, and S-mC-1.0, indicating their mesoporous structures. This indicates that thiophene not only acts as a sulfur doping precursor but also influences the morphology of the mesoporous carbon material. Low-angle X-ray diffraction (XRD, Figure 1r) further confirmed the ordered structure of the material and highlighted the amorphous nature of the carbon skeleton.[17] Moreover, wide-angle XRD characterization of S-mC-0.25, S-mC-0.5, and S-mC-1.0 can be seen from Figure S4, the diffraction patterns consistently revealed a broad (002) peak centered at approximately 23° (2θ) across all samples, confirming the amorphous carbon frameworks. Therefore, the sulfur heteroatoms in thiophene moieties may establish secondary bonding interactions with both the hydroxyl groups of phenolic resin and the poly(ethylene oxide) segments of F127 surfactant (Figure S5). This interfacial modification could perturb the micellar packing geometry, potentially compromising pore uniformity. The hydrophobicity of thiophene can disrupt the hydrogen-bonding network between the surfactant and resin matrix, thus destroying the order of pore structure.

The porosity of the material was analyzed using nitrogen adsorption technology. The nitrogen adsorption–desorption isotherm of S-mC-x exhibited a noticeable hysteresis loop in the middle-high pressure range ($P/P_0 = 0.4$–0.8, as shown in Figure 2a), indicating the presence of mesopores and macropores. The BJH method calculated the pore size to be approximately 2–5 nm, consistent with observations made using transmission electron microscopy. Moreover, a sharp increase in the isotherm at low pressures suggests the presence of numerous micropores (< 2 nm) within the material, aligning with the pore size distribution findings. The abundance of microporous structures can improve the specific surface area, influencing heteroatom doping configurations and catalytic performance. Figure 2c illustrates that the maximum specific surface area of S-mC-0.375 is 829 m^2 g^{-1}, surpassing that of S-mC-0.5 and S-mC-1.0. This porous structure not only boosts the specific surface area for enhanced exposure of active sites during electrocatalysis but also enables rapid diffusion of O_2 in the catalyst and the efficient desorption of H_2O_2 products. Consequently, this material facilitates the acceleration of $2e^-$-ORR while preventing excessive reduction of H_2O_2, thanks to its unique pore structure featuring large mesopores and macropores simultaneously.
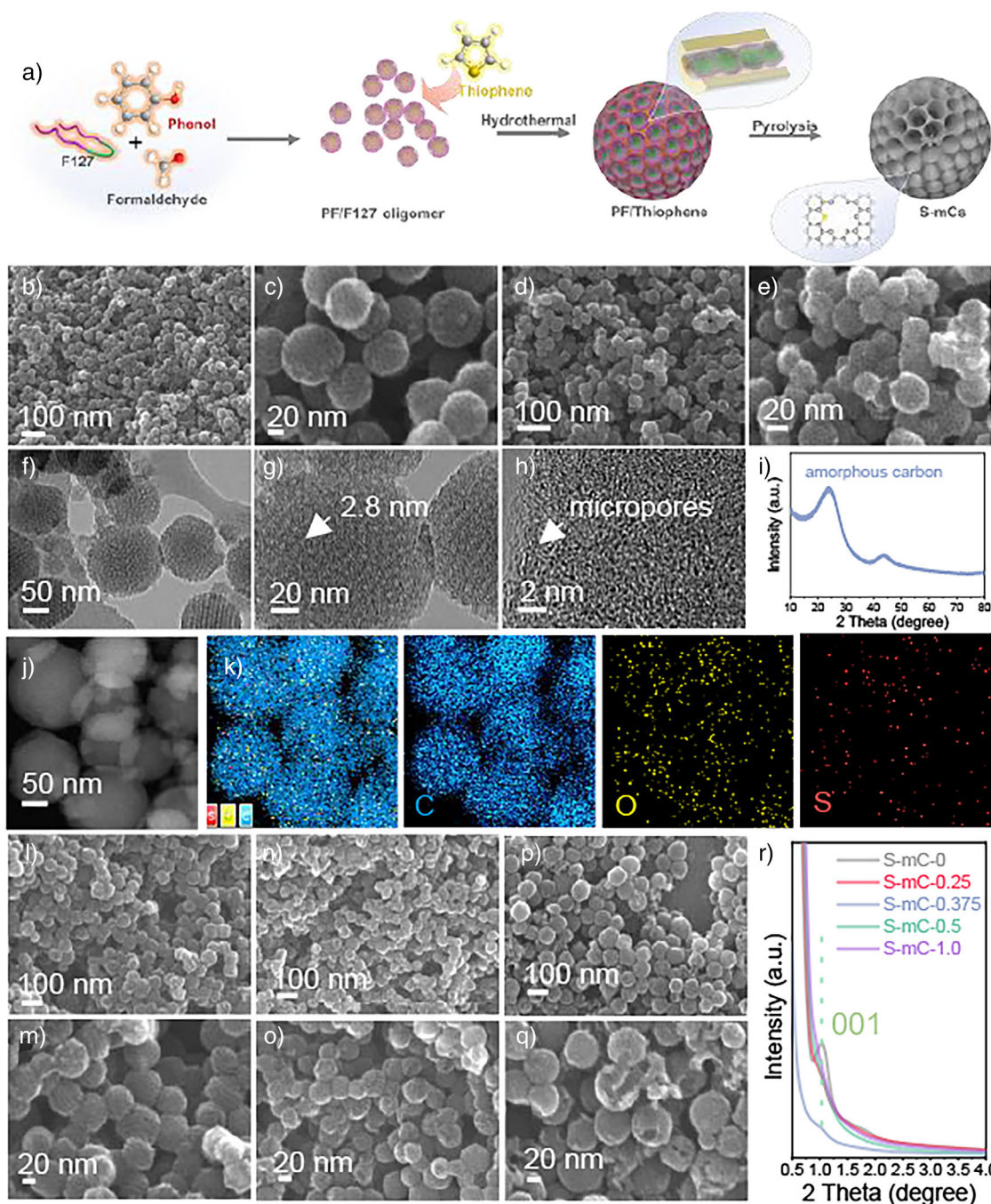
Figure 1. a) Schematic illustration of the synthesis of S-mC; b,c) SEM image of S-mC-0, d,e) SEM images, f–h) TEM images, i) wide angle XRD, j) STEM images, and k) EDS mapping of S-mC-0.375, l,m) SEM images of S-mC-0.25, S-mC-0.5 (n,o), and p,q) S-mC-1.0; r) low-angle XRD of S-mC samples.

X-ray photoelectron spectroscopy (XPS) was performed. Carbon, nitrogen, and sulfur can be found in the measurement scan of S-mC-x (Figure S6). Despite the progressive increase in thiophene precursor loading, the sulfur content in S-mC-x composites remained nearly constant (Figure 2d). This invariability strongly indicates that sulfur incorporation into the resin-derived carbon skeleton approaches a doping saturation threshold under the applied synthesis conditions. As shown in Figure 2e, the C 1 s spectrum is at 284.6, 285.1,

and 288.6 eV, which can be attributed to C═C, C═N/C and C─O, respectively. The measured S2p spectrum displays two characteristic peaks corresponding to thiophene S (Figure 2f), which indicates an edge doping configuration of S atoms on the carbon skeleton.[18,19] O1s spectrum of S-mC samples at 531.1 and 533.2 eV can be attributed to C═O and C─O (Figure S7).

Further structural information of the materials was then acquired through Raman spectroscopy, revealing two distinct
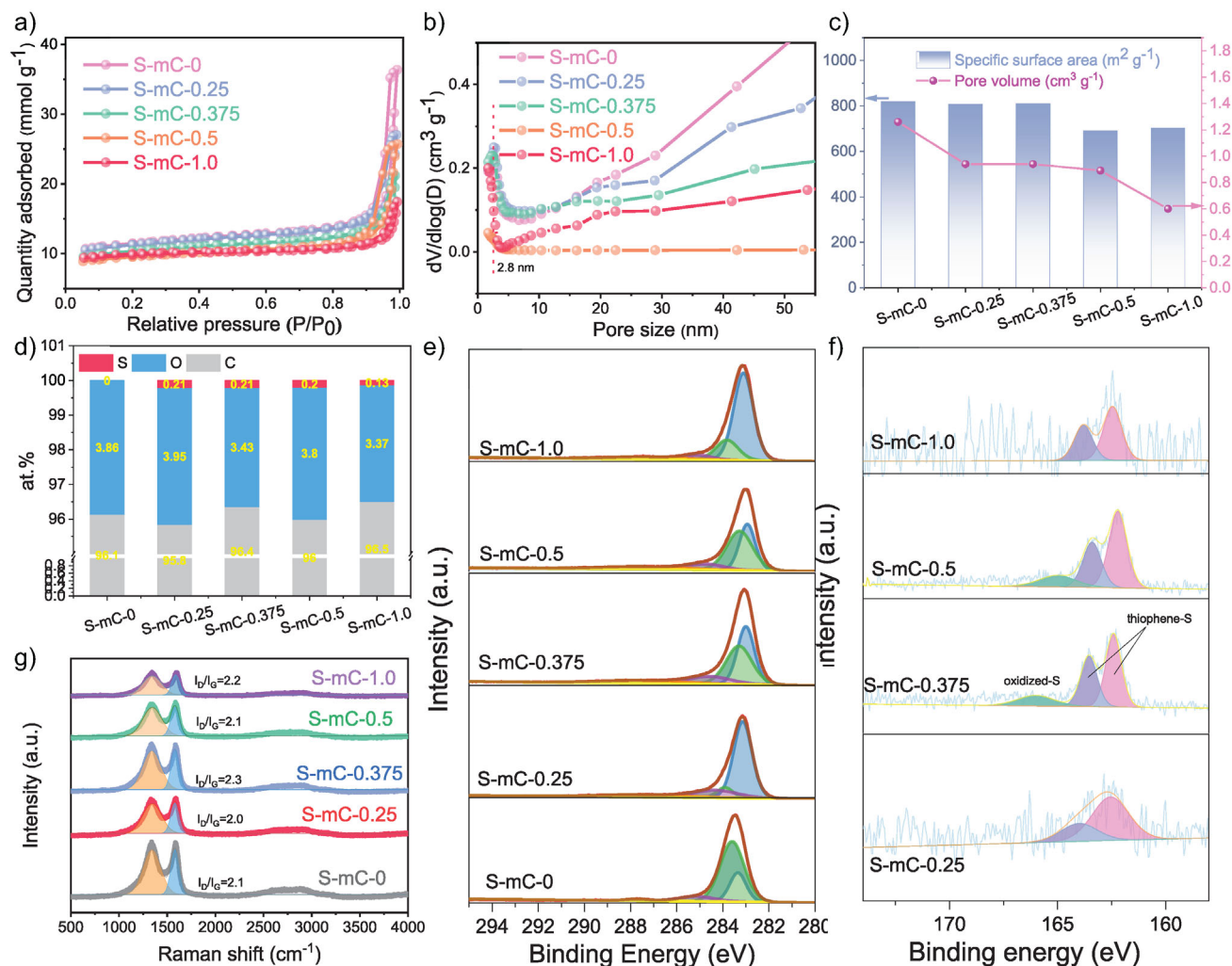
Figure 2. a) N_2 adsorption/desorption isotherms, b) pore size distribution of S-mC-x samples; c) specific surface area and pore volume of S-mC-x samples; d) Comparison of S, O and C content ratio of mC-x samples; e) XPS of C1s and f) S2p of S-mC samples, g) Raman spectroscopy of S-mC-x samples.

bands at 1300 and 1580 cm^{-1}, as depicted in Figure 2g. These bands correspond to the lattice/edge defects (referred to as the D band) and the in-plane stretching vibration of the sp^2 hybridized carbon atoms (known as the G band) within the carbon framework. The relative intensity of these bands, known as the D to G ratio, provides valuable insights into the defect content of the material. By analyzing the Raman data and fitting it to the respective bands, it was observed that S-mC-0.375 exhibited the highest I_D/I_G ratio of 2.3 among the S-mC-x samples, indicating the highest defect content.[20] This abundance of defects in S-mC-x is believed to be linked to the ample pore structure introduced by the F127 soft template. The elevated defect content of the carbon spheres obtained can be attributed to a combination of multiple factors.

The electrocatalytic performance of the materials for 2e$^-$-ORR was evaluated in a 0.1 M KOH aqueous electrolyte. The cyclic voltammetry (CV) curves of S-mC-x in N_2- and O_2-saturated electrolytes are shown in Figure 3a. In the O_2-saturated electrolyte, the CV curve of S-mC-x displays a distinct ORR current at approximately 0.6 V versus RHE,

indicating its capability for catalyzing ORR. Linear sweep voltammetry (LSV) was then conducted on a rotating ring-disc electrode to further evaluate the 2e$^-$-ORR performance of the materials. The LSV curves in Figure 3b show that S-mC-0.375 exhibits the largest ring current and the smallest disk current, suggesting its preference for the 2e$^-$-ORR pathway. In contrast, the undoped S-mC-0 sample shows inferior ORR performance and H_2O_2 selectivity (Figure S8). This underscores the importance of sulfur doping in enhancing the 2e$^-$-ORR process. The H_2O_2 selectivity and electron transfer number of the samples were plotted against the testing potential in Figure 3c. Remarkably, S-mC-0.375 demonstrated an H_2O_2 selectivity of around 100%, corresponding to an electron transfer number of approximately 2.01 (Figure 3d), the highest among all samples tested. Additionally, S-mC-0.375 achieved a disk current density of 1.1 mA cm^{-2} at 0.65 V versus RHE, close to the equilibrium potential for 2e$^-$-ORR, indicating efficient ORR kinetics with minimal overpotential for O_2-to-H_2O_2 conversion. Interestingly, the sulfur content did not significantly improve the selectivity for

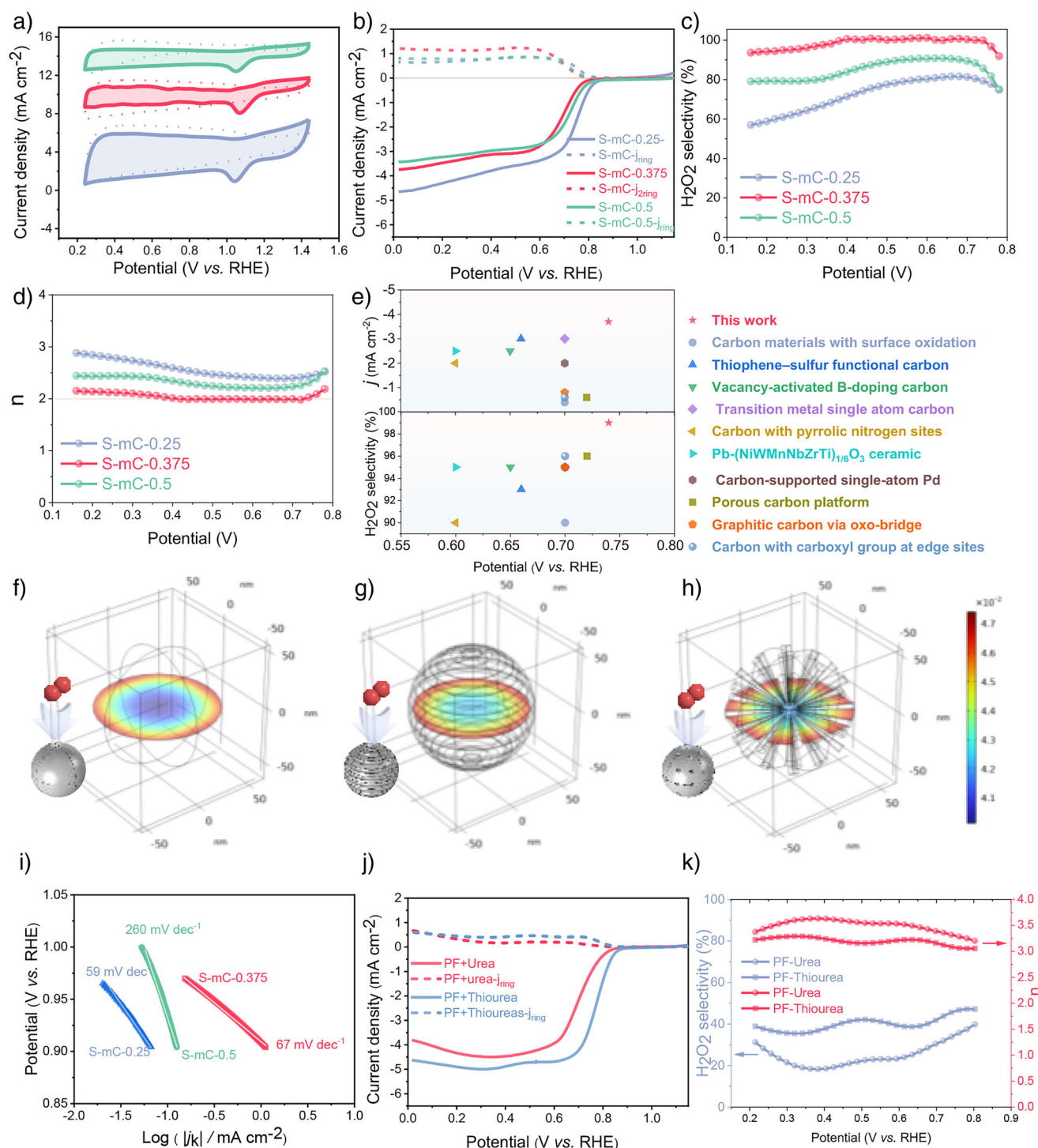*Angew. Chem. Int. Ed.* **2025**, *64*, e202503385 (4 of 9)

© 2025 Wiley-VCH GmbH

Figure 3. a) CV curves of S-mC-x in O_2 and N_2-saturated 0.1 M KOH solution. b) LSV curves of S-mC-x samples, showing the current densities on the disk (j_{disk}) and ring (j_{ring}) electrodes. c,d) H_2O_2 selectivity and electron number of the materials. e) Comparison of H_2O_2 selectivity and ORR activity in 0.1 M KOH between S-mC-0.375 and previously reported catalysts. f–h) Spatial distribution of O_2 concentration over different pore structures. i) Tafel plots derived from LSV curves. j) LSV curves of different samples with N-doped and N/S doped mesoporous spheres, tested at 1600 rpm and a rate of 5.0 mV s^{-1}, showing the current (densities) on the disk (j_{disk}) and ring (j_{ring}) electrodes. k) H_2O_2 selectivity and electron number of the N-doped and N/S doped mesoporous spheres.

$2e^-$-ORR in the S-mC-x analogues, as depicted in Figure 3d. Overall, the electrochemical tests establish that S-mC-0.375 exhibits exceptional $2e^-$-ORR selectivity, which correlates positively with its well-structured pore arrangement and sulfur doping. Obviously, the S-mC-0.375 catalyst displayed exceptional ORR catalytic activity and H_2O_2 selectivity in 0.1 M KOH (Figure 3e and Table S1), outperforming most previously reported catalysts, such as B-doped carbon, N-doped carbon, and especially S-doped carbon.[11,19,21–33] By removing the F127 from the mesoporous resin reaction system, we successfully prepared sulfur-doped carbon spheres (S-CS, Figure S9) without mesopores to confirm the role of the carbon sphere's pore structure in the $2e^-$-ORR process. Nitrogen adsorption/desorption analysis (Figure S10) along with Raman analysis (Figure S11) confirmed the micropore structure and amorphous carbon structure of the CS. XPS analysis (Figure S12) further confirmed the sulfur doping. However, the LSV test (Figure S13) revealed poor $2e^-$-ORR performance and low H_2O_2 selectivity over S-CS.

In the ORR process, the transport of oxygen on the catalyst is a crucial role in determining its performance. To confirm this phenomenon, three finite element simulation configuration models representing S-mC-0 without obvious pores, S-mC-0.25 with transverse parallel channel, and S-mC-0.375 with vertical cylindrical pores (Figure S14) were built to compare the oxygen transport capacity of different pores (Figure 3f,h and Figures S15 and S16). The results show that the vertical cylindrical pores have the strongest transmission capacity and can significantly enhance the activity of ORR (Figure S17). To verify the dual effects of this method on sulfur doping and ordered mesoporous maintenance, two alternative approaches for preparation of S-doped carbon spheres. As shown in Figure S18, direct thiophene addition to precursor solutions yielded disordered mesoporous structures with inferior ORR performance (50% selectivity, $j = -1.9$ mA cm^{-2}). Post-synthesis impregnation achieved merely 0.1 at% S incorporation due to thiophene volatility, resulting in similarly poor catalytic activity (Figure S19). Moreover, the positive effect of ordered vertical cylindrical pores for the enhancement in $2e^-$-ORR can be confirmed by commercial carbon Vulcan (0.4 at% S), S-doped carbon nanotube, and S-doped graphene oxide. The disordered pore architecture of commercial carbon Vulcan manifested significantly reduced performance (55% selectivity, Figure S20) relative to our ordered mesoporous catalysts. S-doped CNTs and graphene oxide (0.2 at% S) exhibited limited $2e^-$-ORR activity (<55% selectivity, Figure S21).

Figure 3i displays the Tafel slopes of S-mC-x, with S-mC-0.375 showing a low value of 67 mV dec^{-1}, indicating its fast reaction kinetics. Tafel plots showcase different rate-determining steps (RDS), with a gradual reduction in Tafel slopes suggesting a change in the RDS from the initial electron-transfer step ($O_2 \rightarrow$ *OOH, ~120 mV dec^{-1}) to the final H_2O_2 desorption step (*OOH $\rightarrow H_2O_2$, ~70 mV dec^{-1}).

In this study, we focus on the synergistic effect of sulfur doping and an ordered vertical cylindrical pore structure, which play a crucial role in enhancing the $2e^-$-ORR process. Mesoporous carbon samples doped with nitrogen, as well as co-doped with both sulfur and nitrogen were involved

to highlight the significance of sulfur doping. The nitrogen-doped mesoporous carbon (PF-urea) was synthesized by introducing urea into the reaction system of mesoporous PF resin. The mesoporous carbon spheres obtained exhibited a distinct mesoporous structure, as depicted in Figure S22. Further characterization through nitrogen adsorption/desorption (Figure S23) and Raman analysis (Figure S24) confirmed the mesoporous structure and amorphous carbon skeleton. XPS analysis (Figure S25) also provided evidence of successful nitrogen doping. The $2e^-$-ORR performance of PF-urea was evaluated using LSV. As shown in Figure 3j,h, PF-urea displayed a preference for the 4e-ORR process, with a selectivity to H_2O_2 of only 20%. Thiourea was introduced into the reaction system of mesoporous PF resin, resulting in the preparation of sulfur–nitrogen co-doped mesoporous carbon spheres (PF-thiourea). The SEM and TEM images of PF-thiourea (Figure S26) reveal a clearly visible ordered cylindrical pore structure, indicating that PF maintains the assembly structure without disruption like thiophene. The experimental results from nitrogen adsorption/desorption (Figure S27) and Raman analysis (Figure S28) further confirm that PF-thiourea possesses a rich mesoporous structure and amorphous carbon framework like S-mC. XPS analysis (Figure S29) delves into the nitrogen and sulfur doping on the surface of PF. As depicted in Figure 3g,h, the LSV test conducted demonstrated PF-thiourea 4-electron ORR performance and highlighted the significant role of pure sulfur doping in the $2e^-$-ORR process. Moreover, the inclusion of different amounts of thiourea validated the results that an increase in content leads to the destruction of the original pore structure, akin to the effects of thiophene doping, as illustrated in Figure S30. Consequently, it is evident that the synergistic effects of sulfur doping and an ordered vertical cylindrical hole structure are crucial factors that contribute to the enhancement of the $2e^-$-ORR effect.

Two finite element simulation models (Figure S31) were also utilized to analyze the distribution of total reducing substances during cyclic voltammetry testing on the S-mC models. The simulated cyclic voltammetry curves of the mesoporous models showed a smaller redox peak difference compared to the solid model (Figure 4a). The current density streamline (Figure S32) shows the faster current distribution of the mesoporous structure. The simulations revealed that the reducing substance distributes uniformly both inside and outside of the catalyst through the mesopores of the models. This indicates that the rich vertical cylindrical pores enhance the accessibility of active sites within the catalyst. As a result, the S-mC electrocatalyst exposes more active sites to the reactant and functions as nano-electrocatalytic reactors to enhance the electrochemical redox reaction of O_2 (Figure 4b,c). This is further supported by the larger electrochemically active surface area (ECSA) of S-mC-0.375 when compared to other catalysts (Figures S33 and S34).

In-situ Raman spectroscopy was utilized to monitor the alterations in the carbon structure of the catalyst throughout the electrolysis process. The potential from 1.2 to -0.2 V versus RHE resulted in a decrease in the intensity of D and G peaks (Figure 4d), potentially caused by the generation of H_2O_2 on the catalyst's surface and partial oxidation of the
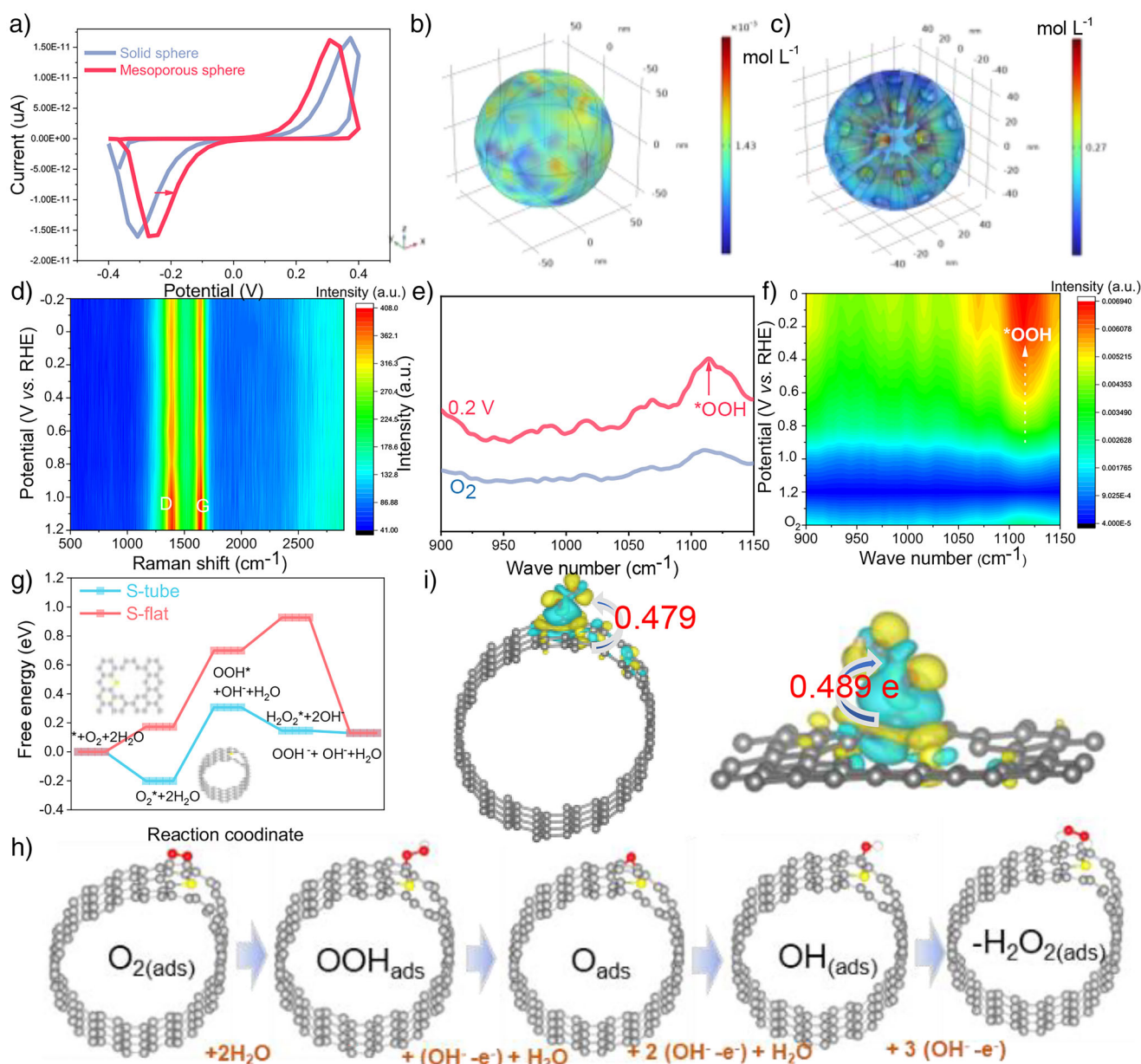
Figure 4. a) CV curves obtained by electrical analysis in finite element analysis, b,c) total reducing substance distribution over S-mC model during electrical analysis of finite element simulation. d) In situ Raman and e,f) infrared spectroscopy test and g–i) free energy diagrams for 2e⁻-ORR reduction. h) Intermediate structures of ORR mechanism on S-tube model.

carbon framework. Moreover, there was no significant change noted in the I_D/I_G ratio, suggesting the overall stability of the catalyst. In situ infrared spectroscopy (Figure S35) was used to test the change of catalyst surface with the change of voltage. Under the voltage of ORR reaction activity, it was clearly observed that the intermediate of *OOH was produced on the catalyst (Figure 4d–f).[34]

Density functional theory (DFT) calculations were used to investigate the energy diagram of the ORR pathway on two distinct types of carbon materials. As shown in Figure S36, the mesopore environment of the catalyst is simulated by using sulfur-containing carbon tubes (S-tube), while the catalyst lacking a mesoporous environment is represented

by a plane sulfur-containing model (S-flat). Based on the free energy curve of 2e⁻-ORR (Figure 4g,h and Figure S37), it is evident that the reduction of adsorbed O_2* species to OOH* is a critical step in the overall reaction. The energy barrier of this key step is shown to be lower than that of the S-flat, highlighting the high 2e⁻-ORR activity of the S-tube.

Charge density difference of S-tube and S-flat with *OOH adsorption is shown in Figure 4i. Yellow and cyan stand for electron accumulation and loss, respectively. Electrons transfers from the support to the OOH*. Bader analysis shows that 0.479 valence electrons and 0.489 valence electrons are transferred away from S-tube and S-flat, respectively.
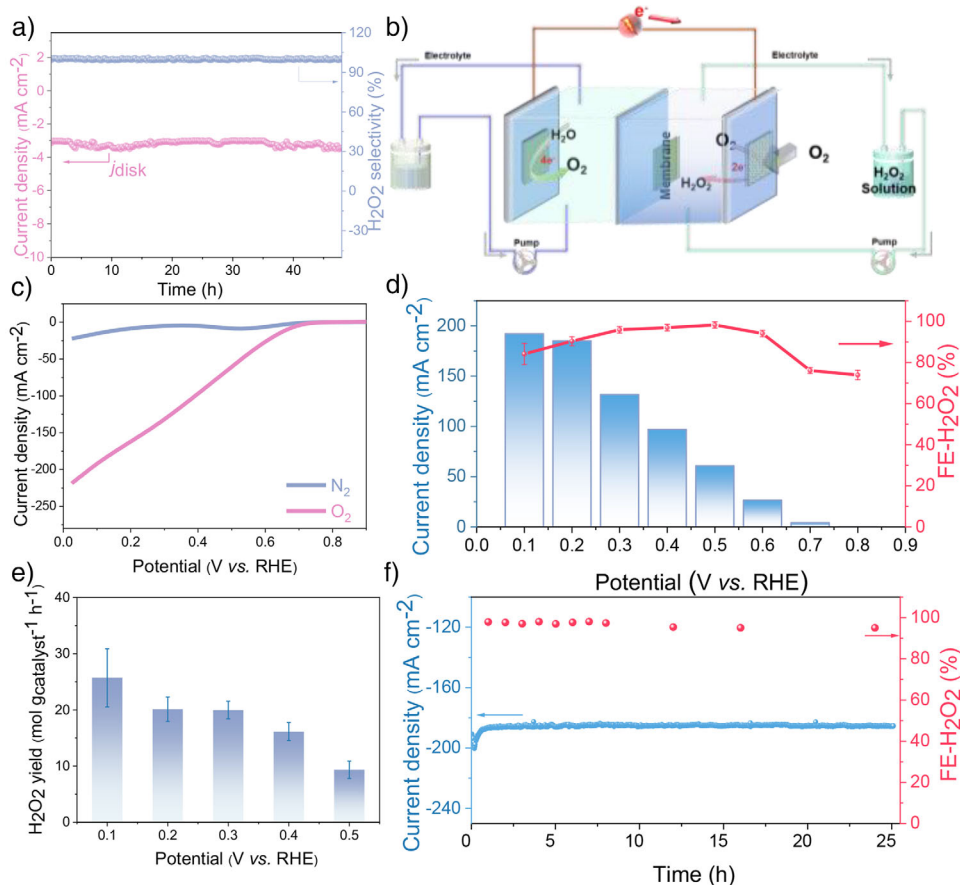
Figure 5. a) Stability evaluation of S-mC-0.375 at a fixed disk potential of 0.4 V versus RHE. b) Schematic diagram of the flow cell setup for H_2O_2 electro-production in neutral electrolyte. c) Polarization curves of S-mC and S-mC in 1 M KOH electrolyte. d) Current densities and FEs of S-mC at various potentials in the flow cell. e) H_2O_2 yield of S-mC at various potentials in the flow cell. f) Chronopotentiometry curve at 0.2 V versus RHE for the H_2O_2 production and H_2O_2 selectivity in flow cell for S-mC.

The performance stability of the S-mC-0.375 catalyst was also demonstrated on RRDE in Figure 5a, with a stable H_2O_2 selectivity of >99% over the 48 h continuous operation. To further assess the practical electro-production of H_2O_2 from S-mC using a flow cell setup (Figure 5b). In the flow cell, S-mC was employed as the cathode, loaded onto a gas diffusion layer, while commercial Pt served as the anode. As shown in Figure 5c, S-mC-0.375 exhibits an onset potential of 0.66 V versus RHE and a sharp increase in current density with rising voltage, reaching -230 mA cm^{-2} @ 0 V vs. RHE, significantly surpassing S-mC-0.375.

Afterward, we conducted time-dependent chronoamperometry tests at various applied potentials to evaluate the capability of S-mC-0.375 for H_2O_2 electro-production. The H_2O_2 produced was quantified using the Ce^{4+} titration method along with ultraviolet-visible spectrophotometry. As illustrated in Figure 5d,e, both the current density and H_2O_2 yield increase as the potential shifts negatively, while the Faraday efficiency (FE) for H_2O_2 production decreases. At 0.2 V versus RHE, S-mC demonstrated a current density of 185 mA cm^{-2} with an FE of ~95%, yielding up to 25 mol $g_{catalyst}^{-1}$ h^{-1} of H_2O_2. Next, we conducted continuous electrolysis for 24 h at a constant voltage of 0.2 V versus

RHE in a 1 M KOH electrolyte. During this period, S-mC exhibited a stable current, a long-term production rate of 25 mol $g_{catalyst}^{-1}$ h^{-1}, and an overall FE of >95% for H_2O_2 electro-production (Figure 5f).

Conclusion

In summary, we have developed S-doped ordered mesoporous carbon spheres through a rational synthetic strategy. The synergistic interplay between S-containing active sites and vertically aligned cylindrical mesopores enables precise modulation of *OOH adsorption configurations. This structural and chemical dual-regulation mechanism substantially lowers the activation energy barrier for the $2e^-$-ORR, thereby establishing an optimized kinetic pathway for selective H_2O_2 generation. The engineered catalyst demonstrates exceptional H_2O_2 production performance, achieving a mass activity of 25 mol $g_{catalyst}^{-1}$ h^{-1} with >95% Faradaic efficiency, while maintaining remarkable operational stability over 24 h of continuous electrolysis. Notably, this work pioneers a multi-site engineering strategy that leverages nonmetallic heteroatom doping and pore architecture design

to manipulate reactant adsorption/desorption thermodynamics. The proposed paradigm not only advances fundamental understanding of structure-property relationships in metal-free electrocatalysts but also provides actionable guidelines for developing cost-effective, durable materials for application-oriented H_2O_2 electrosynthesis systems.

Supporting Information

The authors have cited additional references within the Supporting Information.

Conflict of Interests

The authors declare no conflict of interest.

Data Availability Statement

Research data are not shared.

[1] L. Jing, W. Wang, Q. Tian, Y. Kong, X. Ye, H. Yang, Q. Hu, C. He, *Angew. Chem. In. Ed.* **2024**, *63*, e202403023.

[2] W. Liu, R. Chen, Z. Sang, Z. Li, J. Nie, L. Yin, F. Hou, J. Liang, *Adv. Mater.* **2024**, *36*, 2406403.

[3] Y. Chen, R. Liu, Y. Guo, G. Wu, T. C. Sum, S. W. Yang, D. Jiang, *Nat. Synth.* **2024**, *3*, 998–1010.

[4] S. Chen, T. Luo, X. Li, K. Chen, J. Fu, K. Liu, C. Cai, Q. Wang, H. Li, Y. Chen, C. Ma, L. Zhu, Y.-R. Lu, T.-S. Chan, M. Zhu, E. Cortés, M. Liu, *J. Am. Chem. Soc.* **2022**, *144*, 14505–14516.

[5] Z. Song, X. Chi, S. Dong, B. Meng, X. Yu, X. Liu, Y. Zhou, J. Wang, *Angew. Chem. In. Ed.* **2024**, *63*, e202317267.

[6] Y. Bu, R. Ma, Y. Wang, Y. Zhao, F. Li, G. F. Han, J. B. Baek, *Adv. Mater.* **2024**, *36*, 2412670.

[7] Y.-Y. Yan, W.-J. Niu, W.-W. Zhao, R.-J. Li, E.-P. Feng, B.-X. Yu, B.-K. Chu, C.-Y. Cai, *Adv. Energy Mater.* **2024**, *14*, 2303506.

[8] L. Zheng, Z. Wang, H. Zhang, Y. Shi, F. Wang, Z. Wang, D. Lin, J. Yue, Q. Wang, *Appl. Catal. B* **2024**, *347*, 123811.

[9] M. Fan, Z. Wang, K. Sun, A. Wang, Y. Zhao, Q. Yuan, R. Wang, J. Raj, J. Wu, J. Jiang, L. Wang, *Adv. Mater.* **2023**, *35*, 2209086.

[10] Y. Zheng, P. Wang, W.-H. Huang, C.-L. Chen, Y. Jia, S. Dai, T. Li, Y. Zhao, Y. Qiu, G. I. N. Waterhouse, G. Chen, *Nano Lett.* **2023**, *23*, 1100–1108.

[11] W. Peng, J. Liu, X. Liu, L. Wang, L. Yin, H. Tan, F. Hou, J. Liang, *Nat. Commun.* **2023**, *14*, 4430.

[12] L.-Y. Dong, J.-S. Wang, T.-Y. Li, T. Wu, X. Hu, Y.-T. Wu, M.-Y. Zhu, G.-P. Hao, A.-H. Lu, *Angew. Chem. In. Ed.* **2024**, *63*, e202317660.

[13] P. Cao, X. Quan, X. Nie, K. Zhao, Y. Liu, S. Chen, H. Yu, J. G. Chen, *Nat. Commun.* **2023**, *14*, 172.

[14] C. Zhang, W. Shen, K. Guo, M. Xiong, J. Zhang, X. Lu, *J. Am. Chem. Soc.* **2023**, *145*, 11589–11598.

[15] Q. Zhang, Y. Chen, J. Pan, R. Daiyan, E. C. Lovell, J. Yun, R. Amal, X. Lu, *Small* **2023**, *19*, 2302338.

[16] Q. Tian, L. Jing, H. Du, Y. Yin, X. Cheng, J. Xu, J. Chen, Z. Liu, J. Wan, J. Liu, J. Yang, *Nat. Commun.* **2024**, *15*, 983.

[17] Y. Fang, D. Gu, Y. Zou, Z. Wu, F. Li, R. Che, Y. Deng, B. Tu, D. Zhao, *Angew. Chem. In. Ed.* **2010**, *49*, 7987–7991.

[18] X. Chen, J. Guan, Y. Zheng, Y. Shen, R. Chen, N. Huang, B. Jia, X. Y. Kong, Y. Yan, M. Liu, L. Ye, *Small* **2025**, *21*, 2410619.

[19] R. Xie, C. Cheng, R. Wang, J. Li, E. Zhao, Y. Zhao, Y. Liu, J. Guo, P. Yin, T. Ling, *ACS Catal.* **2024**, *14*, 4471–4477.

[20] S. Zhao, K. Yan, J. Liang, Q. Yuan, J. Zhang, B. Sun, P. Munroe, G. Wang, *Adv. Funct. Mater.* **2021**, *31*, 2102060.

[21] Z. Lu, G. Chen, S. Siahrostami, Z. Chen, K. Liu, J. Xie, L. Liao, T. Wu, D. Lin, Y. Liu, T. F. Jaramillo, J. K. Nørskov, Y. Cui, *Nat. Catal.* **2018**, *1*, 156–162.

[22] W. Cui, Z. Zhen, Y. Sun, X. Liu, J. Chen, S. Liu, H. Ren, Y. Lin, M. Wu, Z. Li, *Angew. Chem. In. Ed.* **2025**,*137*, e202423056.

[23] K. Jiang, S. Back, A. J. Akey, C. Xia, Y. Hu, W. Liang, D. Schaak, E. Stavitski, J. K. Nørskov, S. Siahrostami, H. Wang, *Nat. Commun.* **2019**, *10*, 3997.

[24] Z. Chen, J. Wu, Z. Chen, H. Yang, K. Zou, X. Zhao, R. Liang, X. Dong, P. W. Menezes, Z. Kang, *Angew. Chem. In. Ed.* **2022**, *61*, e202200086.

[25] N. Wang, X. Zhao, R. Zhang, S. Yu, Z. H. Levell, C. Wang, S. Ma, P. Zou, L. Han, J. Qin, L. Ma, Y. Liu, H. L. Xin, *ACS Catal.* **2022**, *12*, 4156–4164.

[26] Z. Deng, M. Gong, Z. Gong, X. Wang, *Nano Lett.* **2022**, *22*, 9551–9558.

[27] Z. Zhang, W. Chen, H. K. Chu, F. Xiong, K. Zhang, H. Yan, F. Meng, S. Gao, B. Ma, X. Hai, R. Zou, *Angew. Chem. In. Ed.* **2024**, *63*, e202410123.

[28] J. S. Lim, J. H. Kim, J. Woo, D. S. Baek, K. Ihm, T. J. Shin, Y. J. Sa, S. H. Joo, *Chem* **2021**, *7*, 3114–3130.

[29] W. Shen, C. Zhang, X. Wang, Y. Huang, Z. Du, M. Alomar, J. Wang, J. Lv, J. Zhang, X. Lu, *ACS Materials Lett.* **2024**, *6*, 17–26.

[30] S. Xu, S. Yu, Y. Xhang, D. Xue, Y. Wei, H. Xia, F. Zhang, J. N. Zhang, *Angew. Chem. In. Ed.* **2024**, *63*, e202407578.

[31] M. Yan, Z. Wei, Z. Gong, B. Johannessen, G. Ye, G. He, J. Liu, S. Zhao, C. Cui, H. Fei, *Nat. Commun.* **2023**, *14*, 368.

[32] Y. Sun, J. Wu, J. Tian, C. Jin, R. Yang, *Electrochim. Acta* **2015**, *178*, 806–812.

[33] F. Wu, J. Nan, Z. Ge, T. Wang, Y. Zhang, X. Ye, B. Liu, *Sep. Purif. Technol.* **2024**, *347*.

[34] Y. Sun, K. Fan, J. Li, L. Wang, Y. Yang, Z. Li, M. Shao, X. Duan, *Nat. Commun.* **2024**, *15*.